A New Spatiotemporal Filtering Method to Reconstruct Landsat Time-Series for Improving Estimation Accuracy of Forest Aboveground Carbon Stock

Kai Huang, Chenkai Teng, Jialong Zhang, Rui Bao, Yi Liao, Yunrun He, Bo Qiu, and Mingrui Xu

***Abstract*—Landsat time-series (LTS) archived the multitemporal hyperspectral images, providing freely accessible and long-term optical data for estimating forest aboveground carbon stock (ACS). Due to LTS carrying noise, there were such issues as bias, outliers, and missing values in ACS estimation. Hence, a new filtering method named terrain-perceive spatiotemporal filtering (TP-STF) was developed to improve the estimation accuracy. In TP-STF, landforms were classified based on the terrain data. A computer-recognizable identifier was generated by perceiving each terrain unit. Combining the discriminative criteria with the spatiotemporal information, the TP-STF adaptively selected performant filtering to reconstruct LTS. Then, the random forests regression (RFR) was employed to estimate ACS of *Pinus densata* in Shangri-La, Yunnan, China. Compared with the other filtering, the TP-STF method's reconstructed LTS had the best modeling accuracy and the highest prediction accuracy, with $R^2 = 0.903$, RMSE $= 17.049$ t/hm^2, $P = 81.080\%$, and rRMSE $= 19.691\%$. The ACS results using TP-STF and RFR were: 6.56 million tons in 1987, 6.44 million tons in 1992, 6.33 million tons in 1997, 6.35 million tons in 2002, 6.72 million tons in 2007, 6.70 million tons in 2012, and 7.04 million tons in 2017. The TP-STF could effectively denoise the LTS images in high-altitude regions, providing a new approach to improve the accuracy of remote sensing-based forest ACS estimation.**

Received 1 November 2024; revised 31 December 2024; accepted 3 February 2025. Date of publication 6 February 2025; date of current version 6 March 2025. This work was supported in part by the National Natural Science Foundation of China under Grant 32260390, in part by "Young Top Talents" Special Project of the High-Level Talent Training Support Program of Yunnan province under Grant YNWR-QNBJ-2020-164, and in part by the Forestry Innovation Programs of Southwest Forestry University under Grant LXXK-2023Z06. *(Corresponding author: Jialong Zhang.)*

Kai Huang and Mingrui Xu are with the College of Soil and Water Conservation, Southwest Forestry University, Kunming 650224, China (e-mail: hk706@swfu.edu.cn; 15184850308@swfu.edu.cn).

Chenkai Teng, Jialong Zhang, Yunrun He, and Bo Qiu are with the Key Laboratory of Forest Resources Conservation and Utilization in the Southwest Mountains of China Ministry of Education, Kunming 650233, China, also with Key Laboratory of National Forestry and Grassland Administration on Biodiversity Conservation in Southwest China, Kunming 650233, China, and also with Yunnan Provincial Key Laboratory for Conservation and Utilization of Inforest Resource, Southwest Forestry University, Southwest Forestry University, Kunming 650233, China (e-mail: tckswfu@swfu.edu.cn; jialongzhang@swfu.edu.cn; heyunrun@swfu.edu.cn; qiubo@swfu.edu.cn).

Rui Bao is with the Institute of Southwest Survey and Planning, National Forestry and Grassland Administration, Kunming 650021, China (e-mail: rui787185290@live.cn).

Yi Liao is with the College of Mechanical and Electronic Engineering, Northwest Agriculture and Forestry University, Xianyang 712100, China (e-mail: ianliao@nwafu.edu.cn).

Digital Object Identifier 10.1109/JSTARS.2025.3539395

***Index Terms*—Aboveground carbon stock (ACS), Landsat time-series (LTS), Shangri-La, terrain-perceive spatiotemporal filtering (TP-STF).**

I. Introduction

FOREST aboveground carbon stock (ACS) is a significant indicator that reflects the reserve of carbon elements in forest ecosystems, which is the result of the accumulation of forest ecosystems over many years. Forest aboveground biomass (AGB) is an important indicator reflecting the structure and function of forest ecosystems, which is the result of the long-term production and metabolism of forest ecosystems [1]. The study of forest ACS is based on the research of forest AGB [2]. The research and analysis of ACS are of great significance to the study of global climate change and the terrestrial carbon cycle [3]. With the implementation of the International Geosphere–Biosphere Program (IGBP) in the mid-late 20th century, the productivity and AGB of forest ecosystems have been studied worldwide [4], [5]. The IGBP made scholars in Europe and the United States [6], [7], [8] gradually began to focus on the study of forest carbon stock. It provided valuable reference data for forest ACS estimation. At the beginning of the 21st century, researchers [9], [10], [11], [12], [13] also entered the culmination stage of research on forest carbon stock estimation at the national scale.

The main methods of AGB/ACS estimation include the field survey method and remote sensing-based estimation method [14]. Despite the field survey method having high accuracy, it is difficult to accomplish for large-scale determination of forest AGB/ACS. With the development of remote sensing technology, especially the unique advantages of Landsat satellite data and its correlation with forest carbon stock [15], it is possible to apply this emerging technology to estimate forest ACS at a large scale. Compared with single-period remote sensing images, the advantages of Landsat time-series (LTS) include long-term continuity and less impact of seasonal variations. However, due to the long temporal span of LTS is acquired by multiple sensors, there are inconsistencies and various noises [16]. These issues limit the in-depth application of LTS in estimating forest ACS. If the original LTS is not properly filtered and reconstructed, using LTS data for forest ACS modeling reduces accuracy and results in deviations. It will potentially significantly lower the reliability

of the model in estimating forest ACS. Thus, it is necessary to filter the original LTS to obtain high-quality image datasets. The main filtering applied in remote sensing are: Savitzky–Golay (S–G) filtering [17], Harmonic Analysis of Time-Series filtering [18], Whittaker filtering [19], LandTrendr algorithm [20], and Autoregressive Integrated Moving Average model [21]. Traditional filtering methods tended to focus on developing generic algorithms rather than optimizing them for the specific needs of particular fields [22]. In regions with complex landforms, such as China, applying a uniform set of parameters for filtering often did not align with practical realities [22]. Therefore, it is necessary to choose or develop the best filtering method suitable for the field based on different applications [1].

Our study developed a spatial-temporal filtering method—terrain-perceive spatiotemporal filtering (TP-STF). This filtering method used a linear approach that combined the Vondrak smoothing method (temporal filtering), bilateral filtering (spatial filtering), and TD bilateral filtering (spatiotemporal filtering). The first uniqueness of the TP-STF was that the "Terrain-Perceive" was to identify complex landforms by computer pixel-by-pixel. Traditional classification algorithms required spatial continuity, such as the Equal Interval method, Quantile method, and K-means. For a high-altitude research area with complex and spatially discontinuous terrain, the study introduced the geographical detector (GeoDetector) [23] to achieve more precise terrain recognition. The second uniqueness was that "Spatiotemporal Filtering" selected the suitable filtering method based on the characteristics of different terrains in the images. This adaptive approach ensured that the filtering method was highly compatible with the terrain features so that the pixels could achieve optimal denoising and information retention. In addition, it also significantly improved filtering efficiency, particularly in areas with complex terrain or high heterogeneity.

Therefore, the specific objectives of this study include: 1) completing the development of the spatiotemporal filtering method (TP-STF); 2) evaluating the performance of TP-STF in RFR-based ACS estimation; 3) combining RFR and optimized filtering method to reconstruct LTS for mapping ACS of *Pinus densata* in Shangri-La.

II. Study Area and Datasets

A. Study Area

Shangri-La is located between 26°52′–28°52′N and 99°20′–100°19′E, Northwestern of Yunnan, Southwestern of China. Southwest is the second major forest region in China. Shangri-La is in the southeastern margin of the Tibetan Plateau [24], and hinterland of the Hengduan Mountains [25], making it one of the global hotspots for carbon stock research. The general trend of landform is high in the north-west and low in the south-east. Shangri-La has an average altitude of 3459 m and a maximum height difference of 3892 m, with obvious vertical stereo climatic features and rich forest resources. The *Pinus densata* is one of the dominant species in the local area. Its dense forest canopy helps to regulate runoff and purify water through transpiration. As a long-lived species, it can fix and store a large amount of carbon for a long period of time; therefore, it can maintain the dynamic balance of atmospheric carbon dioxide and oxygen. In addition, it plays a great role in the conservation of soil, the maintenance of biodiversity, and the study of global climate change [26].

TABLE I
LTS Data Used in This Study

Sensor type	Time range	Path/Row (Images)		
		40/132	41/132	41/131
Landsat 5 TM	1987 to 2011	48	28	57
Landsat 7 ETM+	2012 to 2013	5	6	1
Landsat 8 OLI	2014 to 2019	10	14	5

B. Datasets

1) Landsat Time-Series: The satellite images were from 1987 to 2019, which were provided by the National Aeronautics and Space Administration (NASA) and the United States Geological Survey (USGS). Due to the problem of Landsat 7 scan line corrector (SLC)-off imagery in 2003, data were obtained from Landsat 5 ETM until 2012 and Landsat 8 OLI after 2013, with gaps filled by Landsat 7 ETM+. Referring to the document written by Roy et al. [27], the different sensors of Landsat were harmonized based on the Google Earth Engine to obtain better consistent LTS data in terms of spectral features.

Precipitation in the study area was concentrated in the summer and autumn. It was difficult to synthesize effectively usable LTS for continuous time intervals. For the generation of annual composite images, the long time span would include too many complex phenological factors, especially for vegetation [28]. Thus, we selected images with cloud cover less than 10% from January 1 to March 31 and generated the annual composite images using median compositing. The median compositing method sorted all image values for each pixel within the time frame and selected the middle value as the composite value for that pixel, thereby reducing the impact of outliers.

Due to the screening period being in winter and spring, there were areas within the study area covered by snowfall or permanent snow. The ice, cloud, and cloud shadow were screened based on FMASK algorithm that is provided in the Landsat quality assessment band (QA band) [29]. The basic information on LTS is given in Table I.

2) Permanent Sampling Plots: Permanent sampling plots of *Pinus densata* were obtained from the National Forest Inventory (NFI) program with a time distribution of seven periods from 1987 to 2017 at five-year intervals. The permanent sampling plots were surveyed during the seven periods with a total of 136 records (see Fig. 1). The size of each permanent plot is 28.28 m × 28.28 m. Permanent sampling plots of NFI were standardized according to the "Technical regulations for continuous forest inventory" [30]: 1) For the determination of the number of trees, the count for trees with a diameter at breast height (DBH) $\geq$ 8 cm must be accurate. For trees with a DBH $<$ 8 cm, a 5% margin of error is acceptable. 2) For DBH measurement, the acceptable error for trees with a DBH $\geq$ 20 cm is less than 1.5%. For trees with a DBH $<$ 20 cm, the acceptable error is less than

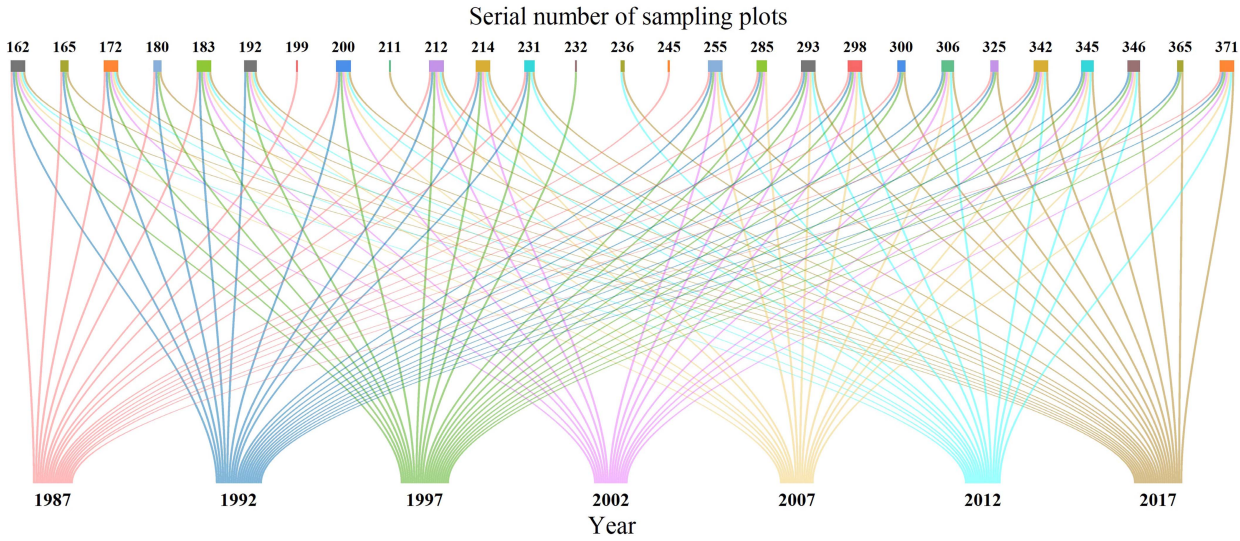

Fig. 1. Sampling plot data records in different survey years.

0.3 cm. 3) For tree height measurement, the acceptable error is less than 3% for trees with a height $<$ 10 m. For trees with a height $\geq$ 10 m, it is less than 5%.

The biomass factor model (1) [31] for *Pinus densata* was used to calculate individual tree AGB

$$\mathrm{AGB} = 0.073 \times \mathrm{DBH}^{1.739} \times H^{0.880} \tag{1}$$

where AGB is the aboveground biomass of individual tree, DBH is the diameter at breast height of the individual tree, and H is the tree height of the individual tree.

The carbon content coefficients of different tree species types are different [32]. In this study, the carbon content coefficient of *Pinus densata* was 0.501 [33]. It was calculated as follows:

$$\mathrm{ACS} = \mathrm{AGB} \times C_c \tag{2}$$

where C_c is the carbon content coefficient of *Pinus densata*.

3) Digital Elevation Model (DEM): The DEM was obtained from the Shuttle Radar Topography Mission (SRTM) Version 3 product, which was provided by SRTM program at NASA's Jet Propulsion Laboratory. Resolution of 1 arc s ($\sim$30 m).

III. Methods

A. Geographical Detector

GeoDetector is an algorithm for detecting and exploiting spatial stratified heterogeneity [23]. In this study, GeoDetector was used to partition various types of landforms. The formula is as follows:

$$q = 1 - \frac{\sum_{h=1}^{L} \sum_{i=1}^{N_h} \left(y_{hi} - \bar{y}_h\right)^2}{\sum_{i=1}^{N} \left(y_i - \bar{y}\right)^2} \tag{3}$$

where q is the result of GeoDetector, $h = 1, \ldots, L$ denotes the number of each type of landforms, y_{hi} is the radiometric value of the image for landform type h, $\bar{y}_h$ is the mean radiometric value of the image for landform type h, y_i is the overall radiation value of the image, and $\bar{y}$ is the average of the overall radiation values of the image.

B. Vondrak Smoothing Method

The Vondrak smoothing method's basic idea is to select a smoothing factor ε to choose a compromise curve between absolute fitting and absolute smoothing of the time-series, removing noise in the image. The calculation formula is as follows [34]:

$$Q = F + \lambda^2 S = \frac{1}{n} \sum_{i=1}^{n} p_i (y_i - y_i')^2 + \frac{\lambda^2}{n-3} \sum_{i=1}^{n-3} \left[\Delta^3 y_i'\right]^2 \tag{4}$$

where Q is the smoothing criterion, F is the degree of fit, S is the roughness, p_i is the sequence of weights, y_i is the time-series data, and y_i' is the sequence of smoothing values. The error curve method was used to select ε [34].

1) The image is filtered using different smoothing factors. The mean-squared error (MSE) (5) of the smoothed values is calculated under each smoothing factor as

$$\sigma_\varepsilon = \sqrt{\frac{\sum_{i=1}^{N} \left(y_i' - y_i\right)}{N-3}} \tag{5}$$

where σ_ε is the MSE of the filtered smoothed value, y_i' is the filtered value, y_i is the observed value, N is the length of LTS, and $N-3$ is to correct the degree of freedom.

2) Plot the curve with the smoothing factor as the abscissa and MSE as the ordinate. Select the smoothing factor that minimizes MSE as the optimal smoothing factor ε.

C. Bilateral Filtering

Bilateral filtering is a nonlinear spatial domain filtering. It combines the influence of the spatial distance and brightness of the pixel within the filter window by multiplying the two Gaussian kernels. Thus, it effectively smooths images while preserving edge information. The formula is as follows [35]:

$$F(i,j) = \frac{\sum_{k,l} I(k,l)\, w(i,j,k,l)}{\sum_{k,l} w(i,j,k,l)} \tag{6}$$

where (i, j) is the coordinate of the filtering pixel. (k, l) is the coordinate of the neighboring pixel within the filter window. F is a filtered image. I is an unfiltered image. $w(x, y, k, l)$ is the weight coefficient of the filter window, which is the product of the spatial domain kernel and the value domain kernel of the Gaussian function

$$w(x, y, k, l) = \exp\left[-\frac{(i-k)^2 + (j-l)^2}{2\sigma_d^2} - \frac{||v(i, j) - v(k, l)||^2}{2\sigma_r^2}\right] \tag{7}$$

where σ_d is the variance of the spatial domain kernel and σ_r is the variance of the value domain kernel.

D. Temporal-Difference (TD) Bilateral Filtering

In mountainous areas with large elevation changes, there were often sudden changes in terrain features. The texture of the sudden changes was complex. The bilateral filtering tended to "blur" it or cause distortion of edges. Since landform changes remained relatively stable over short time periods, we incorporated pixel information from adjacent years into the filter window to enhance the reconstruction of filtered pixels.

The improvement provided better reconstruction for pixels with sudden changes. Even if the sudden changes were significantly smoothed, it could appropriately reconstruct the image details using pixel information from neighboring years. Specifically, by introducing the TD term $(t-m)^2$, the algorithm was extended into a TD bilateral filtering capable of accounting for spatiotemporal variations. It assumed that the filtered pixel and the pixel in the filtering window not only had spatial coordinate (i, j) and (k, l) but also a time coordinate t and m representing, respectively, the year of the filtering pixel and the pixel in the filter window. Then, the weights needed to combine the spatial distance and the temporal variation of the value range. Therefore, the weight coefficient was improved as follows:

$$F(i_t, j_t) = \frac{\sum_{k_m, l_m} I(k, l, m)\, w(i_t, j_t, k_m, l_m, t, m)}{\sum_{k_m, l_m} w(i_t, j_t, k_m, l_m, t, m)} \tag{8}$$

where (i_t, j_t) is the coordinate of the filtering pixel in t year, (k_m, l_m) is the coordinate of the neighboring pixel within the filtering window in m year, $m \in [t+2,\ t-2]$

$$w(i_t, j_t, k_m, l_m, t, m) = \exp\left[-\frac{(i_t - k_m)^2 + (j_t - l_m)^2 + c^2(t-m)^2}{2\sigma_d^2} - \frac{||I(i, j, t) - I(k, l, m)||^2}{2\sigma_r^2}\right] \tag{9}$$

where c^2 is used to balance the weights of spatial and temporal distances. In this study, we chosen $c = 1$.

E. Terrain-Perceive Spatiotemporal Filtering

Smoothing is a key method for image denoising [36]. However, it inevitably affects the spatial continuity and variability of the reconstructed imagery. For images obtained from high-altitude mountainous areas, the basic assumption of the TP-STF method is that noise and noise-sensitive areas are typically concentrated in specific landforms. Hills or mountainous terrains with a rugged surface often become concentrated areas of noise in the image, whereas relatively flat plains tend to have less noise. Hence, the TP-STF method applies different filtering intensities and parameters for different landforms, seeking a balance between smoothing denoising and preserving spatial features. There are algorithmic processes (see Fig. 2).

1) The relief degree of land surface (RDLS) is obtained from the DEM using a 3×3 neighborhood window. Based on Table II, the RDLS and DEM data are used to classify the fine-scale landforms of the study area.
2) The GeoDetector is used to partition the fine-scale landforms. The q-statistic is matched with the image pixel-by-pixel by spatial location as an identifier for the TP-STF. After matching the classification results with the partitioning results, we obtain the q-statistic intervals for each landform.
3) Based on the q-statistic, the TP-STF reconstructs LTS as follows.
   a) *q-statistic is less than 0.7:* The topographic features are relatively continuous, with no distinct boundaries. The TP-STF method employs the Vondrak smoothing method. Since flat areas inherently have less noise, a low-parameter temporal filtering approach with gentle smoothing was sufficient to improve data quality without affecting the spatial continuity.
   b) *q-statistic is between 0.7 and 0.8:* The landforms are mainly composed of low-to-medium altitude hills with some undulations but good spatial continuity. For such areas with moderate topographic complexity, using high-parameter temporal filtering will cause oversmoothing and result in image distortion. The TP-STF method employs the low-parameter bilateral filtering to denoise by interpolation, thereby preserving the spatial variability of the imagery.
   c) *q-statistic is between 0.8 and 1.0:* The landforms are composed of high altitude hills or mountains. Due to the significant pixel value fluctuations caused by noise, a small number of flat areas are also classified into this range. Both situations are considered regions with significant noise effects. The TP-STF method employs TD bilateral filtering. It flexibly assigns weights based on the differences in temporal and spatial information of pixels while smoothing denoising and reconstructing surface texture details. The reconstructed images can retain spatial continuity and variability even after filtering.
4) Output reconstructed LTS images.

F. Principle of Filtering Methods for Comparison

The study selected traditional temporal filtering and spatial filtering (S–G filtering and MF), improved temporal filtering and spatial filtering [BSTS and adaptive topography convolution (ATC)], as well as single temporal filtering and spatial filtering

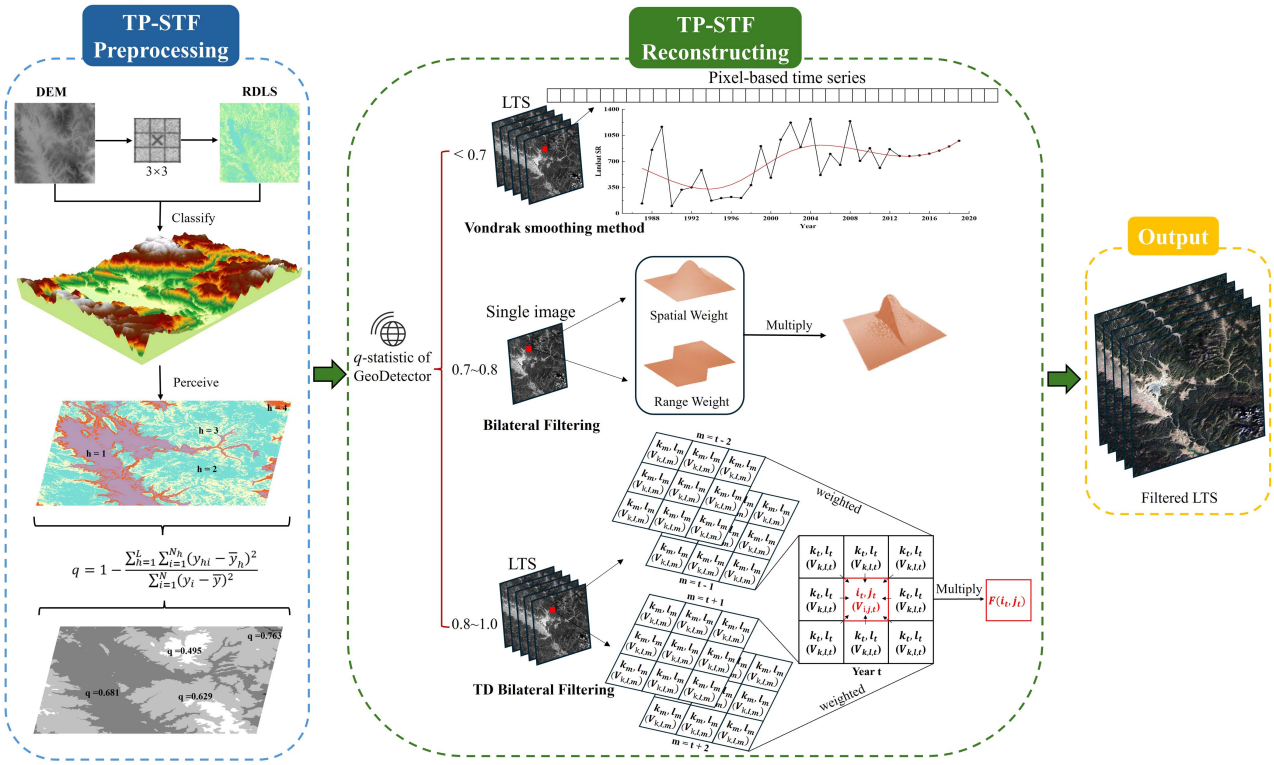

Fig. 2. Flow of the TP-STF.

TABLE II
[37] CLASSIFICATION OF LANDFORMS

Undulation / Elevation	Low-Altitude (<1000 m)	Medium-Altitude (1000–3500 m)	High-Altitude (3500–5000 m)	Very High Altitude (>5000 m)
Plain (<30 m)	low-Altitude Plain	Medium-Altitude Plain	High-Altitude plain	Very High Altitude plain
Hill (30–200 m)	Low-Altitude hill	Medium-Altitude hill	High-Altitude hill	Very High Altitude Hill
Mountain (>200 m)	Low Mountain	Middle Mountain	High Mountain	Very High Mountain

(Vondrak smoothing and Bilateral filtering) for comparison and analysis with the TP-STF.

1) Savitzky–Golay Filtering: The S–G filtering is a polynomial fitting method based on the least squares approach [17]. By controlling the window size, the original LTS is fitted using polynomial weighting to remove noise [38]. The smaller the window size, the closer to the true value.

2) Mean Filtering (MF): The MF is a nonlinear filtering method based on order statistics theory [39]. It arranges the pixels within a window and selects the median of these pixels as the filtering result. In this study, the window size was set to 3×3.

3) Best Slope Temporal Segmentation (BSTS): The core idea of the BSTS is to segment a continuous time-series according to the best slope, where the slope of each segment is less than the overall slope before segmentation [40]. LTS reconstruction is achieved by connecting time-series segments. Compared to the best index slope estimation [41], this BSTS is more effective in preserving certain abrupt changes in land cover.

4) Adaptive Topography Convolution Filtering: The ATC combines spatial convolution theory with inverse distance weighting through a linear approach, reconstructing pixels from a spatial domain perspective [42]. It utilizes information from neighboring pixels to eliminate noise-affected regions, thereby enhancing image quality and clarity.

G. Quality Assessment for the Filtered Landsat Time-Series

Root-mean-square error (RMSE) is used to evaluate the difference between the images before and after filtering. Peak signal-to-noise ratio (PSNR) and structural similarity (SSIM) [43] are used as indicators to evaluate the quality of images before and after filtering. PSNR is used to compare the similarity between the filtered image and the original image; SSIM is used to evaluate the quality of the image by the image's luminance, contrast, and structure. The formula is as follows:

$$\mathrm{RMSE} = \sqrt{\frac{\sum_{i=1}^{n} (y_i - y_j)^2}{n}} \tag{10}$$

where y_i denotes the filtered pixel value, y_j denotes the pixel value of the original image

$$\mathrm{PSNR} = 10 \lg \left(\frac{\mathrm{MAX}_f^2}{\mathrm{MSE}} \right) \tag{11}$$

TABLE III
DETAILS OF REMOTE SENSING VARIABLES

Categories	Variables	Meaning/Formula
Original Bands	Blue(B1)	Monitoring of vegetation, soil health.
	Green(B2)	Calculation of various vegetation indices.
	Red(B3)	Monitoring of changes in vegetation growth.
	NIR(B4)	ACS/AGB estimation.
	SWIR1(B5)	Distinguishing bare soil.
	SWIR2(B7)	Forest fire detection.
Vegetation Indices	Normalized Difference Vegetation Index (NDVI)	(NIR-Red)/(NIR+Red)
	ND32	(Red-Green)/(Red+Green)
	ND54	(SWIR1-NIR)/(SWIR1+NIR)
	ND57	(SWIR1-SWIR2)/(SWIR1+SWIR2)
	ND452	(NIR+SWIR1-Green)/(NIR+SWIR1+Green)
	Atmospheric Ratio Vegetation Index (ARVI)	(NIR-(2×Red-Blue))/(NIR+(2×Red-Blue))
	Chlorophyll Index (CI)	(NIR/Green)-1
	Difference Vegetation Index (DVI)	(NIR-Red)
	Enhanced Vegetation Index (EVI)	2.5×((NIR−RED)/(NIR+6×RED−7.5×BLUE+1))
	Leaf Area Index (LAI)	(3.618×EVI−0.118)
	Normalized Burn Ratio (NBR)	(NIR-SWIR2)/(NIR+SWIR2)
	Relative Vegetation Index (RVI)	NIR/Red
	Soil-Adjusted Vegetation Index (SAVI)	(NIR-Red)×(1+L)/(NIR+Red+L) , L is 0.25
	Vegetation of Atmospheric Resistance Index (VARI)	(NIR-(2*RED-BLUE))/(NIR+(2*RED-BLUE))
	Global Environmental Monitoring Index (GEMI)	eta×(1-0.25×eta)-((Red-0.125)/(1-Red)) eta=(2×(NIR^2-Red^2)+1.5×NIR+0.5×Red)/(NIR+Red+0.5)
	Green Vegetation Index (GVI)	-0.2848×Blue-0.2435×Green-0.5436×Red+0.7243×NIR+ 0.0840×SWIR1-1.1800×SWIR2
Ratio Factor	B4/B2	NIR/Green
	B5/B3	SWIR1/Red
	B5/B4	SWIR1/NIR
	B5/B7	SWIR1/SWIR2
	B7/B3	SWIR2/Red
	B3/albedo	Red/(Blue+Green+Red+NIR+SWIR1+SWIR2)
	B4×B3/B7	(NIR×Red)/SWIR2

where RMSE of the image element with position (x, y) before and after filtering needs to be calculated, $\mathrm{MSE} = \frac{1}{W\times H}\sum_{x=0}^{W-1}\sum_{y=0}^{H-1}\left[f(x,y)-o(x,y)^2\right]$, W and H represent the dimensions of the image; second, the peak value of the image (MAX_f) needs to be counted, $\mathrm{MAX}_f = \left[f_{(0,0)} : f_{(W-1,H-1)}\right]$

$$\mathrm{SSIM}\,(x,y) = l\,(x,y)\cdot c\,(x,y)\cdot\ s\,(x,y) \tag{12}$$

where l, c, and s represent luminance, contrast, and structure, respectively. The image value should be stretched to 0–255 before use.

H. Aboveground Carbon Stock Modeling

1) Variables Selection: Different features of *Pinus densata* have different emitted or reflected radiation characteristics in various bands of Landsat images. The study refers to the remote sensing factors commonly used in AGB estimation [44], mainly including: 6 original bands, 16 vegetation indices, and 7 ratio factors (see Table III). Currently, the Pearson correlation coefficient method is widely used in screening variables [45]. To explore the relationship between remote sensing characteristic variables and the ACS of *Pinus densata*, the method was used to analyze each factor separately and filter out the factors with significant correlations to participate in the modeling.

2) Modeling Method and Accuracy Evaluation: Forest AGB/ACS modeling methods include multiple linear regression and machine learning [46]. Machine learning generally makes fewer assumptions about the data and the process, thus it has higher accuracy than linear regression [47]. The RFR is one of the popular machine learning algorithms. It can standardize the input training data, transforming the data into dimensionless indicators after normalization. At the same time, it effectively addresses the issue of multicollinearity among variables by constructing multiple decision trees [48], [49]. The advantage of RFR lies in its ability to reduce the risk of overfitting due to its insensitivity to changes in parameter values [50]. Some studies have demonstrated that RFR has good predictive capabilities in forest AGB/ACS estimation [51], [52]. With reference by Fassnacht et al. [53] on the sample size required for remote sensing-based estimation of forest biomass, 80% of the records were randomly selected for modeling, while the remaining 20% of the datasets were used for validation.

TABLE IV
SPATIAL PARTITION BY GEODETECTOR

Landforms	q-statistic
Low-Altitude Plain	0.894 - 0.899
Medium-Altitude Plain	0.681 - 0.757
High-Altitude Plain	0.629 - 0.654
Very-High-Altitude Plain	0.849 - 0.898
Medium-Altitude Hill	0.763 - 0.796
High-Altitude Hill	0.495 - 0.704
Very-High-Altitude Hill	0.828 - 0.854
Mountainous area	0.879 - 0.920

Coefficient of determination (R^2) and RMSE (10) were selected as indicators that reflect the model fitting effect. Prediction accuracy (P) and relative root-mean-square error (rRMSE) were used as indicators that reflect the model estimation ability. The following are the formulas:

$$R^2 = \frac{\sum_{i=1}^{n} (\hat{y} - \bar{y})^2}{\sum_{i=1}^{n} (y_i - \bar{y})^2} \tag{13}$$

$$P = \frac{1}{n} \sum_{i=1}^{n} \left(1 - \left| \frac{y_i - \hat{y}}{\hat{y}} \right| \right) \times 100\% \tag{14}$$

$$\text{rRMSE} = \frac{\text{RMSE}}{\bar{y}} \times 100\% \tag{15}$$

where y_i denotes the measured value, $\bar{y}$ denotes the mean value of the measured value, and $\hat{y}$ denotes the model prediction.

I. Standard Deviation Ellipse (SDE)

The SDE is introduced to explore the spatiotemporal distribution of ACS of *Pinus densata*. Different from general spatial statistical methods, the SDE focuses on revealing the global characteristics of the spatial distribution of geographical elements [54]. The SDE is mainly expressed through the center of gravity, spreadability, density, orientation, and shape features [55]. The ACS estimation of *Pinus densata* was used as the corresponding weights, and the first standard deviation number (including 68% of the elements) as the expression range to calculate the SDE of the spatial distribution of ACS. It was implemented based on the spatial statistics module of ArcGIS 10.7.

IV. RESULTS

A. Reconstruction of Landsat Time-Series by TP-STF

The GeoDetector was used to spatially partition the types of landforms in the study area. The range of q-statistics for different landforms was statistically presented in Table IV. It could be found that most landforms had relatively independent intervals of q-statistics. This indicated a better spatial partition with clear classification. Although low-altitude plain and very high altitude plain were generally regions with smooth terrain and low spatial heterogeneity, their q-statistic exceeded 0.8. This suggested that the image areas corresponding to these landform types contained a significant amount of noise, leading to pixel information being contaminated. Subsequently, the q-statistic was used as a computer-recognizable identifier to reconstruct images.

The TP-STF was used to reconstruct LTS from 1987 to 2019 (see Fig. 3). From the visual effect, in Fig. 3(a), (b), and (e), large areas of the missing image were situated in the southwestern region. These areas were mostly high-altitude mountainous areas where year-round snow cover prevented the sensor from acquiring complete image information. The TP-STF could appropriately restore images when high-quality spatiotemporal information was available for the pixels. It aimed to recover the complete imagery of Shangri-La to reduce uncertainty in ACS estimation. One of the sampling plots surveyed in 2012 (No. 342) was in the missing stripes area, roughly within the red box in Fig. 3(f). Fig. 3(h) showed that the missing data at No. 342 was better repaired after filtering; it could avoid the loss of image information that would affect the accuracy of the ACS estimation. Overall, the image quality of LTS after TP-STF reconstruction was upgraded. It was also found that TP-STF had the capability of strip repair.

In the study area from north to south, seven permanent sampling plots [No. 192, No. 212, No. 236, No. 255, No. 293, No. 345, No. 371, marked in yellow in Fig. 4(c)] were selected to show the change of the images before and after the filtering (see Fig. 5) and the time sequence curves (see Fig. 6). For the images after TP-STF method's reconstruction: 1) Plots No. 192 and No.212 had issues with cloud shadows and overly dark imagery. The brightness and clarity of the images were improved after filtering. 2) Plots No. 255 and No. 293 exhibited large missing areas in 1992 and 2007. However, due to the availability of high-quality adjacent spatiotemporal information, the missing images were restored. 3) Plots No. 236, No. 345, and No. 371 were affected by mountain shadows. After filtering, the surface features became sharper.

For the change of time sequence curves, we could find that: 1) the TP-STF method's reconstructed the LTS by fitting a new time-series ("dashed line" in Fig. 6) using the trend of the original time-series ("solid line" in Fig. 6). 2) Plots No. 192, No. 212, and No. 236 had mild fluctuations in the original time-series. The "abrupt changes" in the time-series mainly occurred between 1990 and 1995 and 2005 and 2010, likely caused by winter snowfall in Shangri-La. During the small-scale "sudden changes and recoveries" of values, TP-STF could accurately identify and filter the fluctuations. 3) Plots No. 293, No. 345, and No. 371 had large fluctuations in the original time-series.

We thought that there was a lot of "noise" in the LTS. Denoising was achieved through curve smoothing. Taking Plot No. 293 as an example, it showed significant fluctuations between 1987 and 2012. The "sudden changes" in the spectral curves were generally caused by real surface changes or noise. The ACS records of NFI during 1987 and 2017 (with a 5-year interval) were 12.05 t/hm^2, 13.98 t/hm^2, 14.09 t/hm^2, 19.56 t/hm^2, 20.02 t/hm^2, 15.42 t/hm^2, and 15.70 t/hm^2. The changes in ACS reflected a significant increase in surface vegetation during this period, which stabilized after 2012. The corresponding original spectral curves also exhibited this trend but the large amount of noise caused significant fluctuations in the curves. After fitting

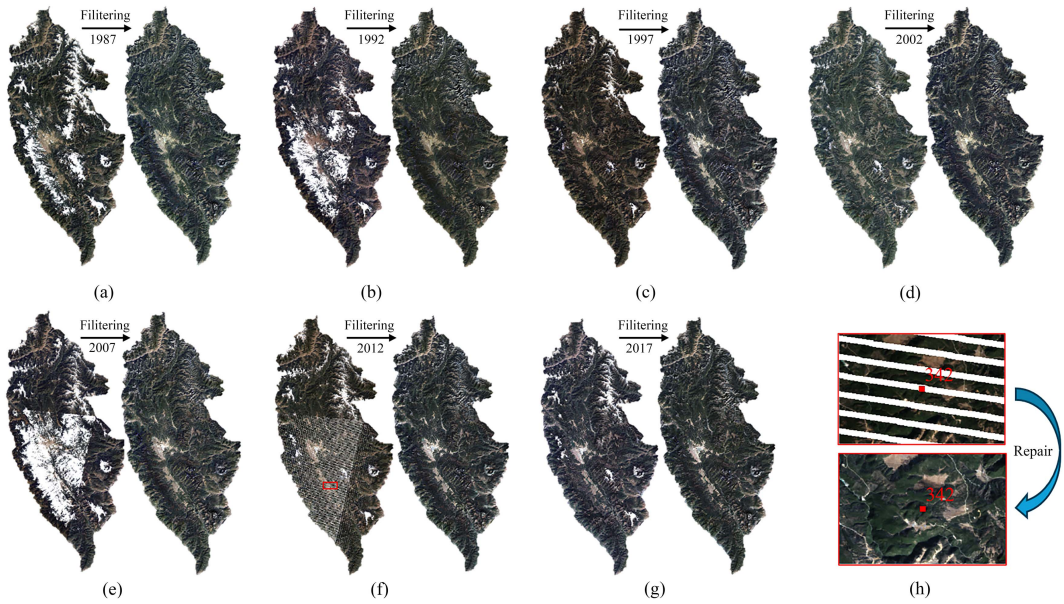

Fig. 3. Filtering results: (a)–(g) left are the unfiltered annual composite images, right are the reconstructed images by TP-STF, and (h) shows the repair for the problem of Landsat 7 SLC-off in 2012.

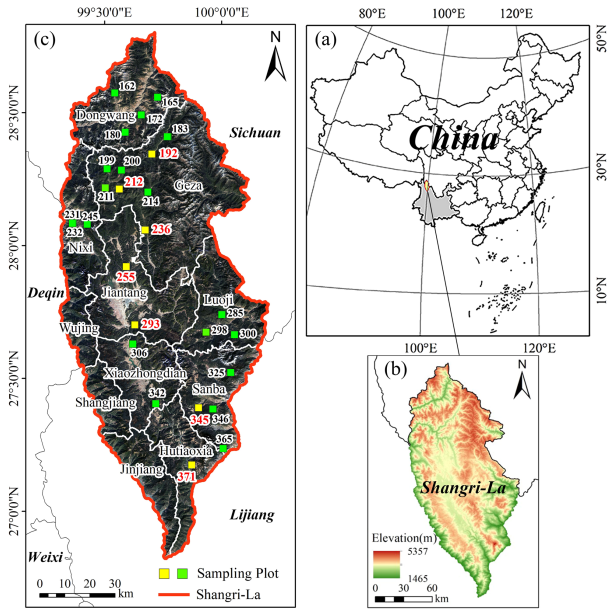

Fig. 4. Study area. (a) Location of Shangri-La in China. (b) Elevation of study area. (c) Distribution of permanent sampling plots of *Pinus densata*.

with the TP-STF, the spectral curves reflected this trend much more accurately. Regarding the sudden increase in ACS between 1997 and 2002 and the stabilization of ACS after 2012, TP-STF effectively preserved these changes in the trend after smoothing to denoise the spectral curves.

B. Image Quality Assessment After TP-STF

The RMSE statistics of the images before and after filtering are performed pixel by pixel (see Table V). The images before and after filtering had a large difference. The NIR band had the largest change, the mean value of RMSE was 301.148, and the standard deviation was 323.945. The Blue band had the smallest change, the mean value of RMSE was 89.945, and the standard deviation was 168.144.

TABLE V
RMSE STATISTICS

Band	Max	Min	Mean	Std
Blue	9786.346	0.21	89.945	168.144
Green	8326.801	0.25	92.912	148.336
Red	10087.713	0.16	102.766	167.175
NIR	8066.253	0.13	301.148	323.945
SWIR1	7703.741	0.13	224.701	307.639
SWIR2	4922.246	0.14	162.701	244.978

Combining PSNR and SSIM to evaluate the quality of the filtered images, as shown in Fig. 7, the PSNR of the filtered images was mostly above 30 dB. It indicated that the distortion of the image quality was less, meaning that the quality of the filtered LTS was more stable and improved. The Green, Red, NIR, and SIWR2 bands fluctuated up and down around 30 dB in 2012. This was because the TP-STF filtering to repair the missing areas of the strips had differences from the original data, thus affecting the PSNR accuracy. The overall fluctuation of the SSIM ranged from 0.6 to 1.0, concentrating in the range of 0.75–0.85, which indicated that the fidelity of the filtered LTS was high.

C. Estimation of Aboveground Carbon Stock

1) Variable Selection and Accuracy Assessment: In comparing the RFR modeling performance of different filtering, the

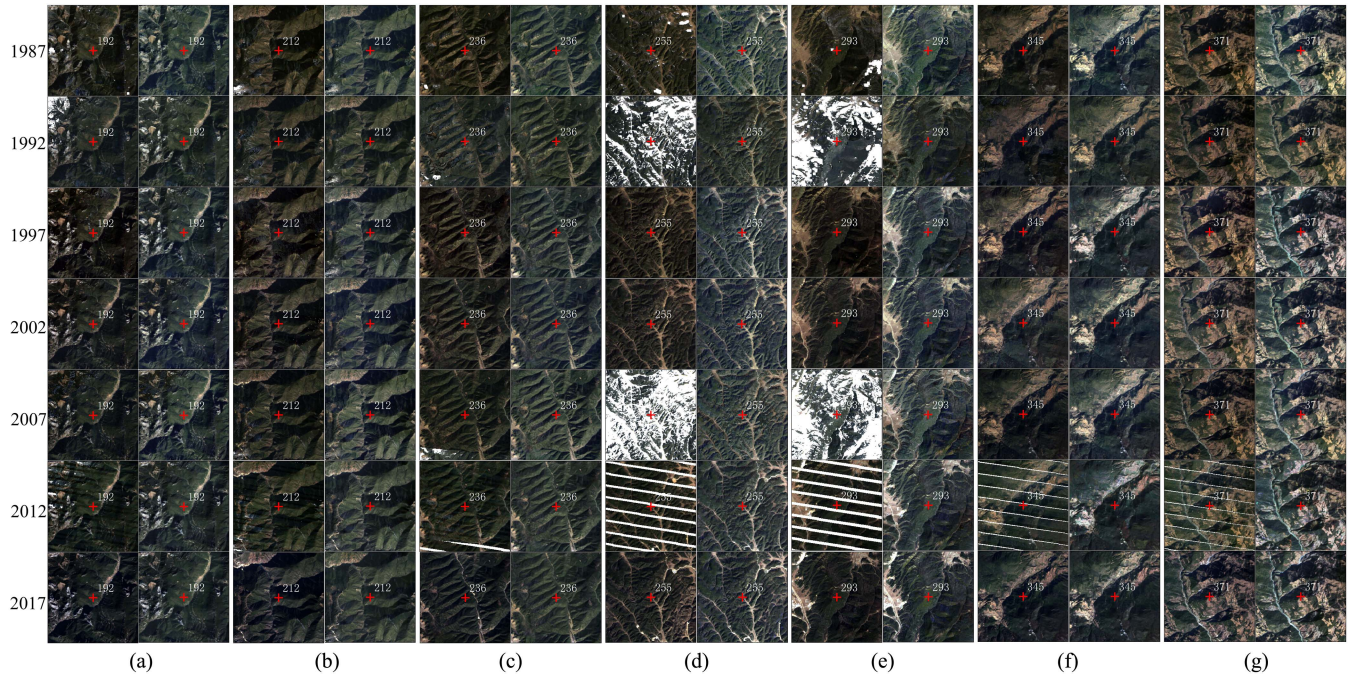

Fig. 5. Comparison of unfiltered and filtered images of seven selected permanent sampling plots (Left: unfiltered; right: filtered; scale of 1:1 000 000). (a) Sampling plot 191. (b) Sampling plot 212. (c) Sampling plot 236. (d) Sampling plot 255. (e) Sampling plot 293. (f) Sampling plot 345. (g) Sampling plot 371.

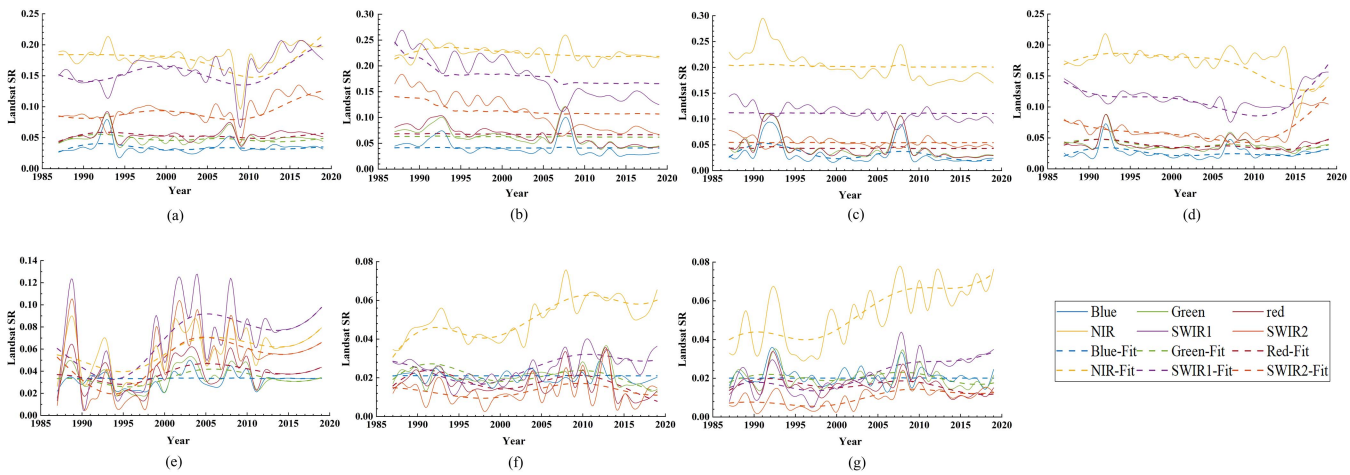

Fig. 6. Algorithmic visual comparison of TP-STF for seven permanent sampling plots. (a) Sampling plot 192. (b) Sampling plot 212. (c) Sampling plot 236. (d) Sampling plot 255. (e) Sampling plot 293. (f) Sampling plot 345. (g) Sampling plot 371.

remote sensing variables were extracted from the LTS before and after filtering (see Table III). The Pearson correlation coefficient method was used to remove variables that showed low correlation with ACS (sig < 0.05 level). Furthermore, some redundant predictors with significant mutual influence (multicollinearity) were eliminated after Pearson correlation analysis considering the significant correlations between variables [56], [57]. Finally, the selected variables for modeling were determined (see Table VI).

The accuracy of the RFR modeling results (see Table VII) indicated that the filtering process could significantly improve the accuracy of ACS modeling compared with the unfiltered LTS. Compared to other filtering methods, the LTS filtered by TP-STF exhibited optimal performance in RFR modeling, with $R^2 = 0.903$, RMSE $= 17.049$ t/hm^2, P $= 81.08\%$, and rRMSE $= 19.691\%$. Next, the TP-STF-fitted LTS was used to estimate ACS.

2) ACS Estimation: Yue et al. [58] found that from November to February of the following year, the net primary productivity of vegetation in Shangri-La reached its lowest point. However, the LTS was acquired during this period. Due to the studied tree, *Pinus densata* (an evergreen conifer) has a smaller needle surface area, usually with a thicker cuticle and wax coating. The environmental factors such as water loss, temperature

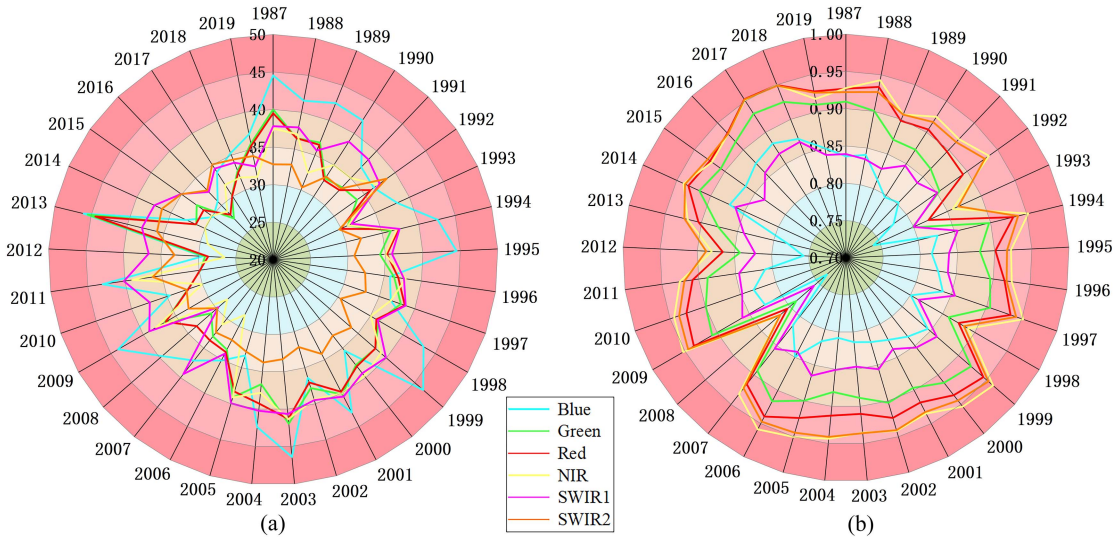

Fig. 7. Image QA. (a) PSNR. (b) SSIM.

TABLE VI
SIGNIFICANT VARIABLES SELECTED OF MODEL BUILDING

Dataset	Variables and Correlation Coefficient
Unfiltered	**LAI**(.351**)、**ND32(**-.192**)、**NDVI**(-.193**)、**ND452**(-.227**)、**B3**(-.204*)、**B4/B2**(-.217*)、**ARVI**(-.222*)、**B1**(-.275*)
Filtered by S-G filtering	**RVI**(.325**)、**SAVI**(.316**)、**NDVI**(.316**)、**CI**(.296**)、**B4/B2**(.296**)、**VARI**(.262**)、**ARVI**(.262**)、**GVI**(.235**)、**B3/Albedo**(-.275**)、**B5/B3**(.184*)、**B5/B4**(-.227*)、**NBR**(.201*)、**ND54**(-.224*)
Filtered by MF	**EVI**(.271**)、**LAI**(.267**)、**B4/B2**(.190*)、**CI**(.187*)、**NDVI**(.184*)、**SAVI**(.184*)
Filtered by BSTS	**NBR**(.317**)、**ARVI**(.312**)、**VARI**(.312**)、**B4/B3**(.193*)、**GVI**(.174*)、**B5**(-.202*)、**B7**(-.215*)、**B3**(-.274**)、**ND32**(-.325**)、**ND54**(-.366**)、**RVI**(.193*)
Filtered by ATC	**B4/B3**(.355**)、**RVI**(.355**)、**B4/B2**(.319**)、**NDVI**(.319**)、**SAVI**(.319**)、**CI**(.319**)、**GVI**(.253**)、**NBR**(.224*)、**ND452**(.215*)、**B5/B4**(-.224*)
Filtered by Vondrak smoothing	**EVI**(.274**)、**LAI**(.274**)、**B4**(-.226**)、**B1**(-.228**)、**B7/B3**(-244**)、**B5/B4**(-.261**)、**ND452**(-.264**)、**ND32**(-.270**)、**B5/B3**(-.276**)
Filtered by Bilateral filtering	**B4×B3/B7**(.268**)、**B3/Albedo**(.240**)、**ND452**(.232**)、**GVI**(-.211**)、**B5/B4**(-.215**)、**B1**(-.235**)、**B4**(-.238**)、**LAI**(-.239**)、**ARVI**(-.240**)、**ND32**(-.340**)
Filtered by TP-STF	**NDVI**(.358**)、**SAVI**(.358**)、**GEMI**(.356**)、**ARVI**(.338**)、**B4/B2**(.322**)、**CI**(.322**)、**ND452**(.318**)、**RVI**(.308**)、**DVI**(.283**)、**B5/B3**(.285**)、**B4**(.255**)、**B3/Albedo**(-.348**)

"**" represents significant correlation at 0.01 level.
" * " represents significant correlation at 0.05 level.

TABLE VII
MODEL EVALUATION

Dataset	Model Evaluation			
	Goodness of Fit		Prediction Accuracy	
	R^2	RMSE (t/hm^2)	P (%)	rRMSE (%)
Unfiltered LTS	0.804	45.721	60.34	42.163
S-G filtering fitted LTS	0.852	36.175	60.88	49.900
MF fitted LTS	0.848	46.906	62.49	46.279
BSTS fitted LTS	0.897	35.155	74.53	40.032
ATC fitted LTS	0.867	25.405	73.89	20.537
Vondrak smoothing fitted LTS	0.876	36.399	68.78	37.438
Bilateral filtering fitted LTS	0.863	26.696	73.17	23.478
TP-STF fitted LTS	0.903	17.049	81.08	19.691

TABLE VIII
ANNUAL ESTIMATION OF PINUS DENSATA

Year	Average/t·hm^{-2}	Total/t
1987	38.234	6559511.984
1992	37.527	6438127.691
1997	37.086	6326545.822
2002	37.246	6353816.749
2007	38.604	6723957.266
2012	38.468	6701603.251
2017	38.090	7039685.249

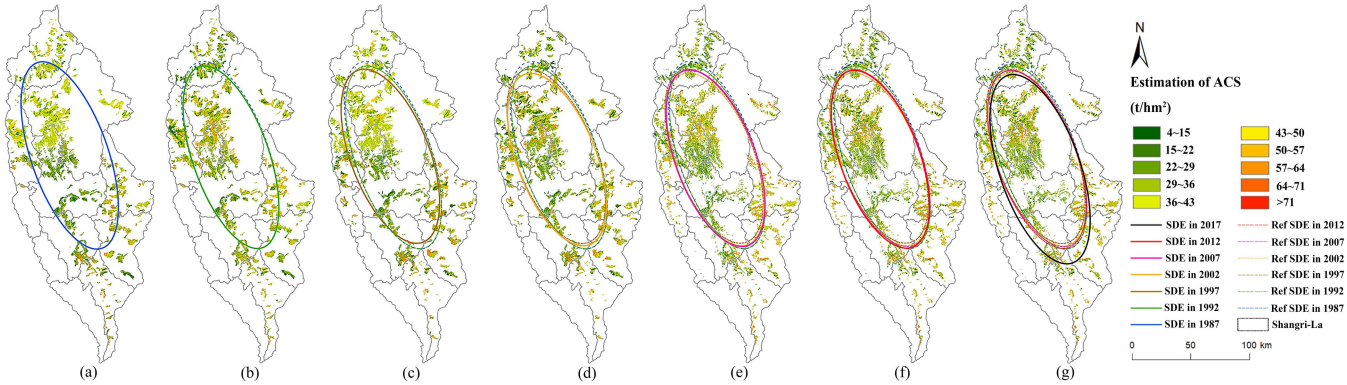

Fig. 8. ACS distribution and SDE of *Pinus densata* in different years. (a) 1987. (b) 1992. (c) 1997. (d) 2002. (e) 2007. (f) 2012. (g) 2017.

decrease, and reduced sunlight have relatively little impact on this species. In addition, coniferous forests, especially evergreen conifer forests, are relatively insensitive to seasonal factors such as temperature and light, and their carbon absorption capacity remained relatively stable [59]. Hence, the ACS was estimated based on RFR, combining TP-STF's reconstructed LTS and sampling plots from the NFI program.

From the ACS estimation of *Pinus densata* in the study (see Table VIII), the total ACS basically maintained an increasing trend from 1987 to 2017, with an increase of about 0.48 million tons. However, there was a decrease in the total ACS of *Pinus densata* from 1987 to 2002. It might be attributed to the presence of regular tending cutting within the Shangri-La woodland. This measure would result in the replacement of mature or overmature forests by young forests, thus affecting the overall stability of the ACS. As China increased the protection of natural forest resources in the Yangtze River Basin starting in 2001 [24], the distribution area of *Pinus densata* in Shangri-La began to increase continuously, which made an increase in total ACS from a decrease to an increase of about 0.69 million tons. Analyzing the average ACS, there was little change in the average ACS over the 30-year period. The reason is that the rising popularity of Shangri-La's tourism led to an accelerating urbanization process. Although the regions of newly planted *Pinus densata*-dominated forests were on the rise during this period, the construction of local infrastructures and the additional *Pinus densata*-dominated forests were still too young. They had a relatively weak carbon storage capacity. This explained why the total ACS of *Pinus densata* increased while the magnitude of change in its average ACS was still relatively stable.

3) Spatiotemporal Variation: The ACS estimation of *Pinus densata* was mapped and overlaid with the SDE over the years (see Fig. 8). The study found that: 1) the ACS distribution showed a spatial pattern of "south (slightly eastward)–north (slightly westward)"; 2) the SDE shape exhibited a "narrow at both ends and wide in the middle," reflecting the concentration of high values of ACS; 3) the spatiotemporal trajectory of the gravity center of SDE showed a southward trend (see Fig. 9), with a total displacement of 16.43 km. Overall, ACS expanded in the south–north direction and contracted in the east–west direction, with the expansion in the south–north direction being stronger than the contraction in the east–west direction. This suggested that the spatiotemporal distribution pattern of ACS of *Pinus densata* in Shangri-La showed obvious evolutionary features, specifically moving southward and expanding spatially.

V. DISCUSSION

A. Performance of the TP-STF in LTS Reconstruction

The study selected Plot No. 255, which is characterized by a high-density distribution of *Pinus densata* and a survey frequency of seven times, to present and analyze the time-series variation of six different spectral curves before and after filtering reconstruction (see Fig. 10). The original spectral curve exhibited significant fluctuations, with noticeable spikes and

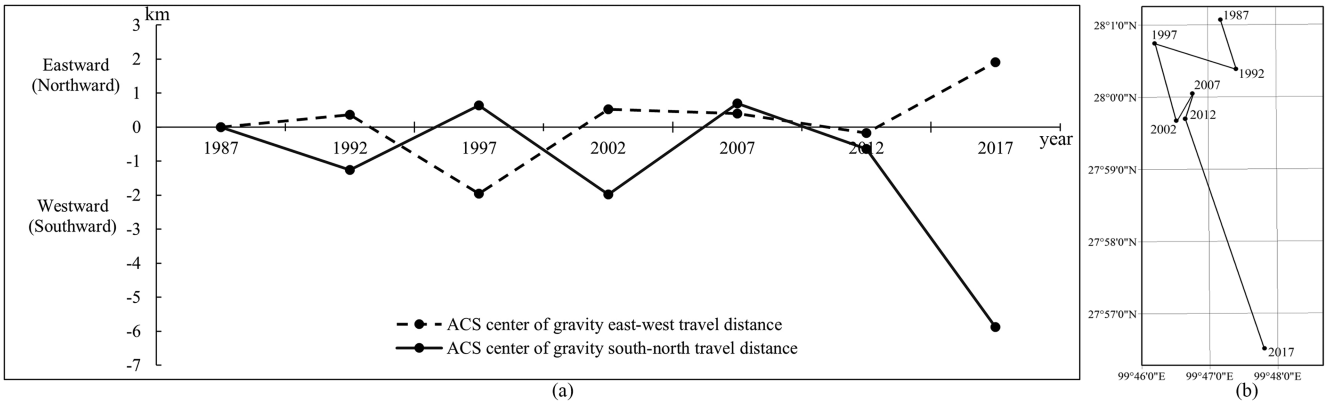

Fig. 9. Changes of ACS centers of gravity displacement, 1987–2017. (a) Displacement direction and distance. (b) Spatial displacement changes.

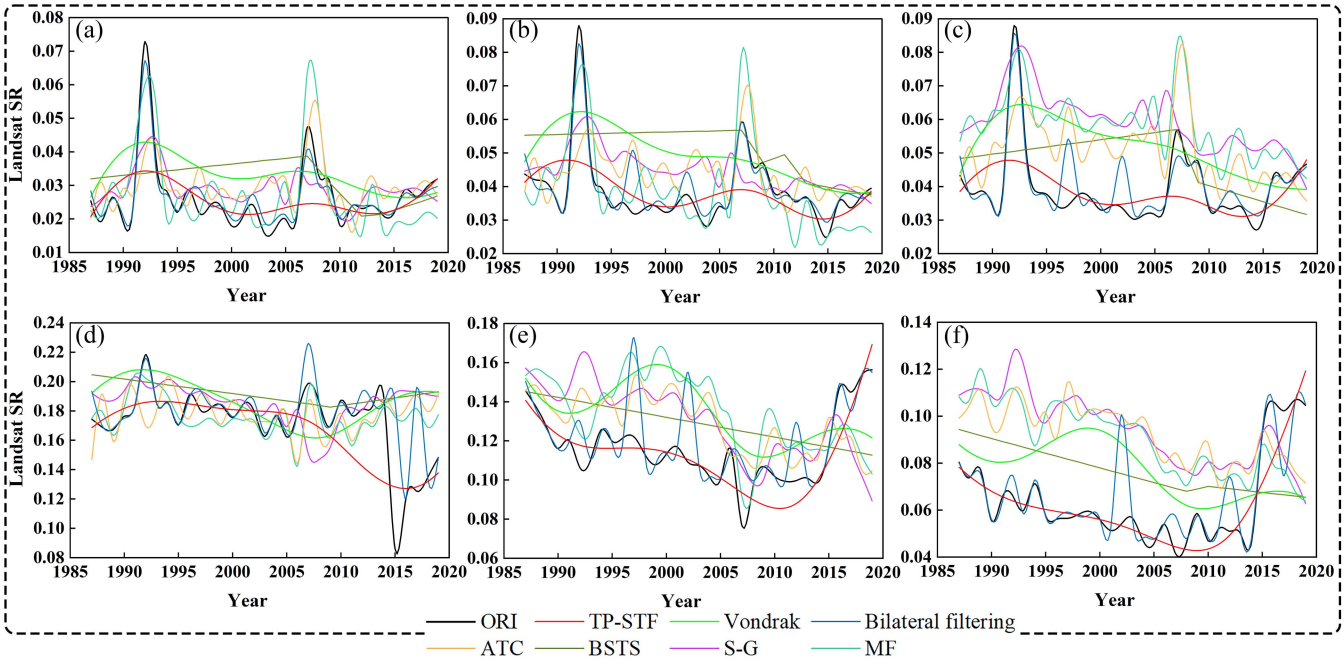

Fig. 10. Spectral curves before and after filtering at sampling Plot No.225: (a) Blue, (b) green, (c) red, (d) NIR, (e) SWIR1, (f) SWIR2.

outliers, indicating that the time-series was heavily influenced by noise. The time-series reconstructed by S–G filtering exhibited a better suitability for smoothing time-series with small fluctuations. However, the S–G filtering was susceptible to the influence of large outliers [the spikes in Fig. 10(a)–(c)], which resulted in a poorer coherence of the overall characteristics of the time-series. The Vondrak smoothing showed a good fit to the long-term trends of the time-series in several bands but there were local fluctuations with large deviations [see Fig. 10(e) and (f)]. The BSTS smoothed fluctuations in the spectral curves using line segments with fewer inflection points. It tracked the trends of the time-series well but it was not effective in fitting "abrupt changes." In addition, it was affected by large abnormal variations [the "abrupt changes" in 2015 in Fig. 10(d)–(f)], leading to an overall high reconstructed surface reflectance. The MF denoised the time-series by using medians. It had a capability in preserving details but the reconstructed time-series still exhibited strong local fluctuations. The bilateral filtering, similar to MF, could preserve more detailed features but it was affected by interference from outliers. Compared to traditional spatial filtering, the ATC filtering was able to reduce the fluctuation amplitude of spike outliers to some extent. However, the time-series fitted by ATC exhibited a certain lag, failing to fully capture the true trend of time-series changes.

Unlike these filtering methods, the TP-STF had following advantages in time-series reconstruction.

1) In Blue band, Green band, and Red band, the TP-STF significantly reduced the spikes and fluctuations in the time-series. It achieved a balance between smoothing the noise and preserving local details by retaining certain curve fluctuations, bringing the time-series within a reasonable range of variation.
2) For the "abrupt changes" in the time-series, the TP-STF exhibited precise tracking of the global trend. The fitted

curve was closer to the overall changes in the original time-series. The TP-STF reduced the effect on the spatial continuity and variability of the reconstructed imagery as much as possible during the filtering process.

3) The time-series fitted by TP-STF did not experience any shift in the overall surface reflectance due to interference from outliers, indicating its robustness.

B. Improvement in ACS Modeling Accuracy Through TP-STF-Fitted LTS

To investigate the improvement in ACS estimation accuracy by TP-STF-fitted LTS, we extracted unfiltered and filtered LTS separately and used them for ACS modeling. From the results (see Table VII), the accuracy of the filtered LTS modeled using RFR outperformed the unfiltered LTS. For the R^2 of the unfiltered LTS was low, while both RMSE and rRMSE were high. It was likely due to the noise in the data, which reduced the model's performance. We further compared the improvement in ACS modeling accuracy using the filtered LTS. The filtered data could the modeling R^2 using the RFR: TP-STF-fitted LTS ($R^2 = 0.903$) > BSTS fitted LTS ($R^2 = 0.897$) > Vondrak smoothing fitted LTS ($R^2 = 0.876$) > ATC fitted LTS ($R^2 = 0.867$) > Bilateral filtering fitted LTS ($R^2 = 0.863$) > S–G filtering fitted LTS ($R^2 = 0.852$) > MF fitted LTS ($R^2 = 0.848$). For the modeling RMSE using the RFR: TP-STF-fitted LTS (RMSE = 17.049 t/hm^2) < ATC fitted LTS (RMSE = 25.405 t/hm^2) < Bilateral filtering fitted LTS (RMSE = 26.696 t/hm^2) < BSTS fitted LTS (RMSE = 35.155 t/hm^2) < S–G filtering fitted LTS (RMSE = 36.175 t/hm^2) < Vondrak smoothing fitted LTS (RMSE = 36.399 t/hm^2) < Unfiltered LTS (RMSE = 45.721 t/hm^2) < MF fitted LTS (RMSE = 46.906 t/hm^2). The filtered LTS showed improvements in fitting performance for RFR, with the best effect achieved using TP-STF-fitted LTS. In addition, the RMSE in RFR using TP-STF-fitted LTS was significantly reduced. However, the modeling performance of MF, Vondrak smoothing, and S–G filtering was less satisfactory, which corresponds to their poorer spectral curve reconstruction results (see Fig. 6). For prediction accuracy, significant improvements were observed in the following modeling results: TP-STF-fitted LTS (P = 81.08%) < BSTS fitted LTS (P = 74.53%) < ATC fitted LTS (P = 73.89%) < Bilateral filtering fitted LTS (P = 73.17%) < Vondrak smoothing fitted LTS (P = 68.78%). Only TP-STF-fitted LTS, with rRMSE = 19.691%, ATC filtering fitted LTS, with rRMSE = 20.537%, and Bilateral fitted LTS, with rRMSE = 23.478%, showed obviously decrease.

The spectral time-series could track the process of vegetation growth and better estimate the AGB and its changes [38]. By establishing a statistical relationship between forest ACS and the spectra of remote sensing images, we could effectively perform remote sensing-based forest ACS estimation. However, the peaks and abrupt fluctuations in the time-series (which might be the "noise") caused the spectral curve fluctuations to fail to accurately reflect changes in ACS. The TP-STF-fitted LTS improved the accuracy of ACS estimation models. This was because TP-STF more comprehensively fitted the nonstationary features in the LTS, providing higher quality input data for ACS estimation and effectively enhancing the accuracy of ACS estimation.

C. Performance of Capturing ACS Change Estimation by TP-STF's Reconstructed LTS

We selected sampling plots where records existed during all seven survey periods of the NFI program to exhibit the performance of TP-STF method's reconstructed LTS in capturing ACS change estimation (see Fig. 11). For Plot No. 255, the NIR, SWIR1, and SWIR2 (the bands are sensitive to vegetation changes in spectral curves) exhibited a downward trend followed by an upward trend [see Fig. 6(d)]. For Plot No. 293, the bands showed a significant increase in spectral curves during 1997–2007 followed by stabilization after 2012 [see Fig. 6(e)]. Combined with the temporal variation of ACS of NFI records, it verified such trends of real surface vegetation change. The TP-STF fitting the trends well by eliminating noise that had significant impacts on interfering with real ground changes. Hence, the reconstructed LTS achieved good reproduction in ACS change estimation, which were close to the survey records. For Plot No. 172, the ACS estimation was generally consistent with the trend of NFI records. It accurately reflects the overall annual increase in ACS. For Plot No. 214, the ACS estimation also closely matched the NFI records. Only at some time points (1987 and 2012), the ACS change estimation had small deviations. Overall, the reconstructed LTS accurately captured the temporal trends of ACS variation in plots, such as continuous ACS increase and significant changes at specific time points.

For sampling plots with significant ACS variation in the NFI records (No. 162, No. 200, No. 298, and No. 342), the reconstructed LTS was also able to capture the temporal variation in ACS change estimation. In the initial year and the period of significant fluctuations (after 2002) of ACS change estimation, the agreement between the estimated values and the NIF survey records was not ideal. Due to the long time span of the NFI survey records, the changes in survey techniques may have introduced uncertainties in the records, which affected ACS change estimation [60]. Moreover, the static ACS estimation model in the study might also affect the accuracy of ACS change estimation. In the future, we will construct a dynamic change model of variation based on TP-STF's reconstructed LTS to further improve the accuracy of ACS change estimation.

D. Comparison With Existing ACS Estimation

To test the validity of ACS estimation in this study, we selected the relevant data of *Pinus densata* from the forest management inventory data in Shangri-La, Yunnan province, China, in 2006 and 2016 for comparison. Meanwhile, we also compared the results of various scholars on the direct estimation of ACS of *Pinus densata* in Shangri-La, as well as the indirect ACS results obtained by using the carbon stock conversion factor (see Fig. 12).

The ACS of *Pinus densata* calculated from forest resource inventory were 6.703 million tons in 2006 and 7.952 million tons in 2016. It was closer to our ACS estimation results in the similar years (2007 and 2017) of the study, with a difference of about 0.021 million tons and 0.912 million tons. The total ACS

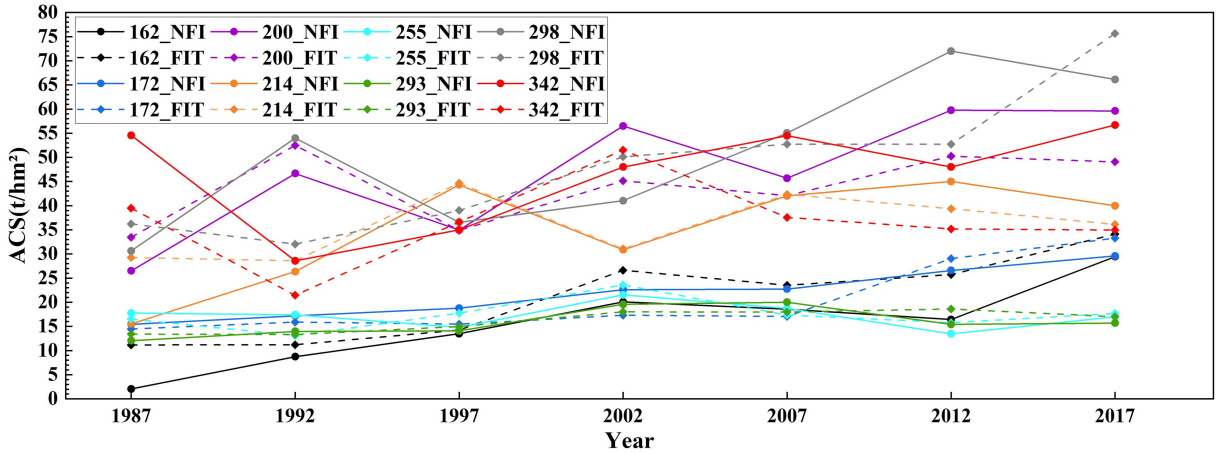

Fig. 11. ACS change estimation by TP-STF's reconstructed LTS: "the solid line" is ACS survey records of the sampling plots from the NFI program, and "the dotted line" is the ACS estimation of the sampling plots after TP-STF's reconstructed LTS.

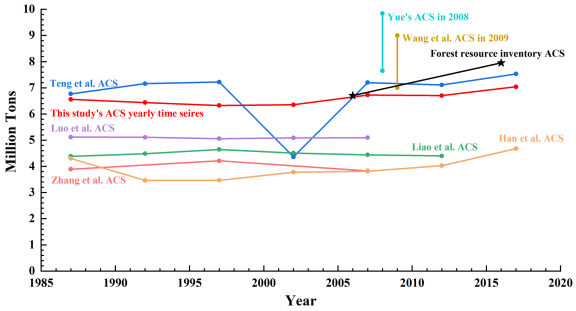

Fig. 12. Comparison estimation studies of ACS of *Pinus densata* by various scholars.

from 2006 to 2016 showed an increasing trend, with an increase of 1.249 million tons. The estimated results of this study also better reflected the rising trend of ACS of *Pinus densata*.

Teng et al. [42] had a great difference in estimating the ACS of *Pinus densata* in 2002 compared to our study (about 1.99 million tons). The differences in results of ACS for the remaining years were relatively small. Han et al. [61] used a nonlinear mixed-effects model for ACS estimation of *Pinus densata*, which generally reported lower results compared to this study (approximately 2.36–2.86 million tons). We used the carbon stock conversion factor to convert AGB to obtain ACS according to other scholars' research results. Yue [62] and Wang et al. [63] focused on forest biomass, which is difficult to compare. Thus, it was necessary to refer to Chen et al.'s [64] study that the AGB for about 70%–90% of forest biomass. We calculated that the ACB of *Pinus densata* in Shangri-La in 2008 studied by Yue was about 7.65–9.84 million tons. The ACS in 2009 studied by Wang et al. was about 7–9 million tons. Zhang et al. [24] and Luo et al. [65] estimated AGB of *Pinus densata* based on LTS. The converted ACS was differed from our study by 6.65 million tons and 2.67 million tons. Due to the wide range of error sources in the estimation process, many subjective and objective factors were difficult to overcome, leading to variations in ACS estimation among different researchers.

E. Limitations and Scalability

In addition to obvious noise, land surface changes, such as deforestation, afforestation, or water body shrinkage, would also cause "abrupt changes" in the time-series. To prevent TP-STF from misidentifying these "abrupt changes" as noise, we selected smaller neighborhood windows to minimize excessive smoothing of the images. However, this made it challenging to balance the weight distribution between spatial and temporal information. Taking the Napahai wetland as an example (see Fig. 13), this region experienced rapid changes in the area within the time window (2015–2019) considered for filtering. Due to the small neighborhood window, the large changes in the area of Napahai wetland in recent years were not accurately captured at the pixel level. Finally, it affected the final filtering results, which was manifested in a significant reduction in the area after filtering. Subsequently, we would incorporate adaptive domain windows into the TP-STF method and establish a spatiotemporal collaboration framework to enhance the algorithm's ability to identify land surface changes and noise.

During the experiment, to verify the accuracy of the terrain classification, test sampling points were not selected in the study area. Instead, the validation was only performed using images or DEM data. It might resulted in the terrain recognition accuracy of TP-STF was low. In the future research, we will do fieldwork to select typical topographical units in different landforms for investigation to reduce the errors caused by visual interpretation. In this way, it aims to improve the terrain recognition accuracy of TP-STF and enhance its filtering performance on the images.

Studies have shown that spectral variation indicators and environmental variables can significantly improve modeling performance [24], [66]. In this research, we focused on the validation and evaluation of the filtering. Hence, we selected a limited set of remote sensing variables to investigate the improvement in ACS estimation accuracy by TP-STF. In subsequent studies, we will integrate more variables to improve model performance of capturing ACS variation.

Fig. 13. Changes in Napahai wetland (red dotted line circle) from 2015 to 2019 and the filtered image in 2017.

VI. Conclusion

We developed the TP-STF to improve the accuracy of forest ACS estimation by reconstructing LTS. This new method integrated the Vondrak smoothing method (temporal filtering), bilateral filtering (spatial filtering), and TD bilateral filtering (spatiotemporal filtering). During the filtering process, the GeoDetector algorithm was introduced to classify the fine-scale types of landforms in the study area. The suitable filtering was applied to reconstruct LTS according to the terrain types. Then, we compared the performance of TP-STF-fitted LTS with the unfiltered filtered and other filtered LTS in modeling ACS. Finally, the TP-STF and RFR were used to estimate the ACS of *Pinus densata*. The results showed the following.

1) In the image QA, TP-STF had a stronger capacity for restoration and enhancement in the LTS image denoising process. The quality of the reconstructed LTS images was significantly improved (PSNR = 26.52–46.49 dB, SSIM = 0.734–0.953).
2) In the LTS reconstruction, the TP-STF struck a balance between smoothing noise and preserving image detail features. The TP-STF-fitted time-series better reflected the vegetation growth fluctuations, and these fluctuations could provide a high-quality dataset for improving ACS estimation accuracy and studying its changes.
3) In the modeling process, the TP-STF-fitted LTS had an optimal performance in RFR. It indicated that the changes of vegetation characteristics over time filtered by the TP-STF-fitted LTS were more in line with the real accumulation and loss of ACS.
4) The estimation results indicated that the ACS of *Pinus densata* did not follow a single trend of continuous increase or decrease but rather exhibited cyclical fluctuations. The result was closer to the actual dynamics of the forest ecosystem [67].

In conclusion, the TP-STF method provided a reference for improving the accuracy of forest ACS estimation in high-altitude areas by denoising in LTS. Due to the unique geographical conditions of Shangri-La, we considered that there were certain limitations in the TP-STF (such as the choice of thresholds and windows). To enhance the transferability, we will incorporate a larger area and other predominant tree species in future research to optimize and improve the TP-STF.

Acknowledgment

All authors would like to thank NASA and USGS for providing Landsat time-series data as well as anonymous reviewers and editors for their comments.

References

[1] C. Teng, J. Zhang, C. Chen, R. Bao, and K. Huang, "Above-ground biomass estimation of *Pinus densata* based on Landsat time series images and AHTC algorithm," *J. Central South Univ. Forestry Technol.*, vol. 44, no. 2, pp. 41–52, Feb. 2024, doi: 10.14067/j.cnki.1673-923x.2024.02.005.

[2] R. B. Mynen et al., "A large carbon sink in the woody biomass of northern forests," *Proc. Nat. Acad. Sci. USA.*, vol. 98, no. 26, pp. 14784–14789, Dec. 2001, doi: 10.1073/pnas.261555198.

[3] Y. Li, M. Li, C. Li, and Z. Liu, "Forest aboveground biomass estimation using Landsat 8 and Sentinel-1A data with machine learning algorithms," *Sci. Rep.*, vol. 10, no. 1, Jun. 2020, Art. no. 9952, doi: 10.1038/s41598-020-67024-3.

[4] E. A. Cook, L. R. Iverson, and R. L. Graham, "Estimating forest productivity with thematic mapper and biogeographical data," *Remote Sens. Environ.*, vol. 28, pp. 131–141, Dec. 1994, doi: 10.1016/S0065-2504(08)60213-5.

[5] E. Rignot, J. Way, C. Williams, and L. Viereck, "Radar estimates of aboveground biomass in boreal forests of interior Alaska," *IEEE Trans. Geosci. Remote Sens.*, vol. 32, no. 5, pp. 1117–1124, Sep. 1994, doi: 10.1109/36.312903.

[6] M. Canell and R. Dewar, "Carbon allocation in trees: A review of concepts for modeling," *Adv. Ecol. Res.*, vol. 25, pp. 59–104, Dec. 1994, doi: 10.1016/S0065-2504(08)60213-5.

[7] D. Zianis and M. Mencuccini, "Aboveground net primary productivity of a beech (Fagus Moesiaca) forest: A case study of Naousa forest, northern Greece," *Tree Physiol.*, vol. 25, no. 6, pp. 713–722, Jun. 2005, doi: 10.1093/treephys/25.6.713.

[8] J. Kellndorfer, W. Walker, E. LaPoint, M. Hoppus, and J. Westfall, "Modeling height, biomass, and carbon in US forests from FIA, SRTM, and ancillary national scale data sets," in *Proc. IEEE Int. Symp. Geosci. Remote Sens.*, Denver, CO, USA, 2006, pp. 3591–3594.

[9] F. G. Alonso, A. R. Zamarron, and J. C. Gozalo, "Assessing forest carbon sinks in Spain using satellite images," in *Proc. IEEE Int. Symp. Geosci. Remote Sens.*, Denver, CO, USA, 2006, pp. 1721–1723.

[10] S. H. Roxburgh, S. W. Wood, B. G. Mackey, G. Woldendorp, and P. Gibbons, "Assessing the carbon sequestration potential of managed forests: A case study from temperate Australia," *J. Appl. Ecol.*, vol. 43, no.no. 6, pp. 1149–1159, Aug. 2006, doi: 10.1111/j.1365-2664.2006.01221.x.

[11] G. Liu, B. Fu, and J. Fang, "Carbon dynamics of Chinese forests and its contribution to global carbon balance," *Acta Ecol. Sinica*, vol. 20, no. 5, pp. 733–740, Sep. 2000, doi: 10.3321/j.issn:1000-0933.2000.05.004.

[12] A. Han, *Study on Monitoring Method of Forest Biomass and Carbon Storage Based on Remote Sensing*. Beijing, China: Beijing Forestry Univ., 2009.

[13] J. Fang, A. Chen, S. Zhao, and L. Ci, "Estimating biomass carbon of China's forests: Supplementary notes on report published in science (291:2320-2322) by Fang et al. (2001)," *Chin. J. Plant Ecol.*, vol. 26, no. 2, pp. 243–249, Mar. 2002. [Online]. Available: https://www.plant-ecol-ogy.com/CN/Y2002/V26/I2/243

[14] L. Torre-Tojal, A. Bastarrika, A. Boyano, J. M. Lopez-Guede, and M. G-raña, "Above-ground biomass estimation from LiDAR data using random forest algorithms," *J. Comput. Sci.*, vol. 58, no. 3, Nov. 2021, Art. no. 101517, doi: 10.1016/j.jocs.2021.101517.

[15] R. D. Spencer, M. A. Green, and P. H. Biggs, "Integrating eucalypt forest inventory and GIS in Western Australia," *Photogramm. Eng. Remote Sens.*, vol. 63, no. 2, pp. 179–181, Feb. 1997.

[16] Z. Zhu, "Change detection using Landsat time series: A review of frequencies, preprocessing, algorithms, and applications," *ISPRS J. Photogramm. Res.*, vol. 130, no. 9, pp. 370–384, Aug. 2017, doi: 10.1016/j.isprsjprs.2017.06.013.

[17] R. Cao et al., "A simple method to improve the quality of NDVI time-series data by integrating spatiotemporal information with the Savitzky-Golay filter," *Remote Sens. Environ.*, vol. 217, pp. 244–257, Nov. 2018, doi: 10.1016/j.rse.2018.08.022.

[18] J. Zhou, L. Jia, and M. Menenti, "Reconstruction of global MODIS NDVI time series: Performance of harmonic analysis of time series (HANTS)," *Remote Sens. Environ.*, vol. 163, no. 15, pp. 217–228, Jun. 2015, doi: 10.1016/j.rse.2015.03.018.

[19] D. Kong, Y. Zhang, X. Gu, and D. Wang, "A robust method for reconstructing global MODIS EVI time series on the Google Earth Engine," *ISPRS J. Photogramm. Remote Sens.*, vol. 155, no. 15, pp. 13–24, Sep. 2019, doi: 10.1016/j.isprsjprs.2019.06.014.

[20] L. Zhu, X. Liu, L. Wu, Y. Tang, and Y. Meng, "Long-term monitoring of cropland change near Dongting Lake, China, using the LandTrendr algorithm with Landsat imagery," *Remote Sens*, vol. 11, no. 10, May 2019, Art. no. 1234, doi: 10.3390/rs11101234.

[21] A. Thavaneswaran and S. Peiris, "Smoothed estimates for models with random coefficients and infinite variance innovations," *Math. Comput. Model.*, vol. 39, no. 4, pp. 363–372, Feb. 2004, doi: 10.1016/S0895-7177(04)90512-2.

[22] R. Li, X. Zhang, B. Liu, and B. Zhang, "Review on methods of remote sensing time-series data reconstruction," *J. Remote Sens.*, vol. 13, no. 2, pp. 335–341, Mar. 2003, doi: 10.11834/jrs.20090257.

[23] J. Wang and C. Xu, "Geodetector: Principle and prospective," *Acta Geo-Graphica Sinica*, vol. 22, no. 2, pp. 116–134, Jan. 2017, doi: 10.11821/dlxb201701010.

[24] J. Zhang, C. Lu, H. Xu, and G. Wang, "Estimating aboveground biomass of *Pinus densata*-dominated forests using Landsat time series and permanent sample plot data," *J. Forestry Res.*, vol. 30, no. 5, pp. 1689–1706, Jun. 2018, doi: 10.1007/s11676-018-0713-7.

[25] L. Tang, L. Gao, and L. Shi, "Sustainable management and protection of ecosystems in Shangri-La county, Yunnan province, China: Introduction," *Int. J. Sustain. Develop. World Ecol.*, vol. 72, no. 1, pp. 99–102, Mar. 2015, doi: 10.1080/13504509.2014.943331.

[26] D. P. Roy et al., "Characterization of Landsat-7 to landsat-8 reflective wavelength and normalized difference vegetation index continuity," *Remote Sens. Environ.*, vol. 185, pp. 55–70, Jan. 2016, doi: 10.1016/j.rse.2015.12.024.

[27] W. Li, *Structure and Spatial Distribution Pattern of Pinus densata Populations in Milin, Southeastern Tibet*. Nanjing, China: Nanjing Forestry Univ., 2023.

[28] R. Bao, J. Zhang, and P. Chen, "Research on improving the accuracy of estimating aboveground biomass for *Pinus densata* based on remote sensing using filtering algorithm," *J. Southwest Forestry Univ.*, vol. 40, no. 5, pp. 126–134, Sep. 2020, doi: 10.11929/j.swfu.201912065.

[29] Y. Fu et al., "SCARF: A new algorithm for continuous prediction of biomass dynamics using machine learning and Landsat time series," *Remote Sens. Environ.*, vol. 314, no no. 1, Dec. 2024, Art. no. 230210, doi: 10.1016/j.rse.2024.114348.

[30] W. Zeng et al., *Technical Regulations for Continuous Forest Inventory of China GB/T 38590-2020*, China, Beijing: Standards press China, 2020.

[31] X. Sun et al., "Modelling of individual tree biomass factors for natural *Pinus densata* forest," *Forest Resour. Manage.*, vol. 3, pp. 49–53, Jun. 2016, doi: 10.13466/j.cnki.lyzygl.2016.03.010.

[32] H. Yang, B. Wu, J. Zhang, D. Lin, and S. Chang, "Progress of research into carbon fixation and storage of forest ecosystems," *J. Beijing Normal Univ.*, vol. 41, no. 2, pp. 49–53, Apr. 2005, doi: 10.3321/j.issn:0476-0301.2005.02.018.

[33] *Guideline on Carbon Stock Accounting in Forest Ecosystem*, Forestry Industry Standard of China LY/T 2988-2018, 2018.

[34] Y. Wu, *The Criterion and the Application of Vondrak Filter*. Hunan, China: Central South Univ., 2012.

[35] C. Tomasi and R. Manduchi, "Bilateral filtering for gray and color images," in *Proc. 6th Int. Conf. Comput. Vis.*, Bombay, India, 2006, pp. 839–846.

[36] J. Pan, X. Yang, H. Cai, and B. Mu, "Image noise smoothing using a modified Kalman filter," *Neurocomputing*, vol. 173, no. 3, pp. 1625–1629, Jan. 2016, doi: 10.1016/j.neucom.2015.09.034.

[37] W. Cheng, C. Zhou, H. Chai, S. Zhao, and B. Li, "Quantitative extraction and analysis of basic morphological types of land geomorphology in China," *J. Geo-Inf. Sci.*, vol. 11, no. 6, pp. 725–736, Dec. 2009, doi: 10.3724/SP.J.1047.2009.00725.

[38] J. Chen, P. Jönsson, M. Tamura, Z. Gu, B. Matsushita, and L. Eklundh, "A simple method for reconstructing a high-quality NDVI time-series data set based on the Savitzky-Golay filter," *Remote Sens. Environ.*, vol. 91, no. 3/4, pp. 332–344, Jun. 2004, doi: 10.1016/j.rse.2004.03.014.

[39] X. Li, W. Zhou, and K. Yang, "An improved method of median filtering algorithm," *Chin. J. Stereol. Image Anal.*, vol. 18, no. 1, pp. 7–1, Mar. 2013, doi: 10.13505/j.1007-1482.2013.01.004.

[40] R. Bao, J. Zhang, C. Lu, and P. Chen, "Estimating above-ground biomass of *Pinus densata* Mast. using best slope temporal segmentation and Landsat time series," *J. Appl. Remote Sens.*, vol. 15, no. 2, Apr. 2021, Art. no. 024507, doi: 10.1117/1.JRS.15.024507.

[41] N. Viovy, O. Arino, and A. Belward, "The best index slope extraction (BISE): A method for reducing noise in NDVI time-series," *Int. J. Remote Sens.*, vol. 13, no. 8, pp. 1585–5190, May 1992, doi: 10.1080/01431169208904212.

[42] C. Teng, J. Zhang, J. Zhang, Y. He, and C. Chen, "Estimation of *Pinus densata* carbon storage based on Landsat time series data and ATC filtering algorithm," *Nature Remote Sens. Bull.*, vol. 28, pp. 2927–2942, 2024, doi: 10.11834/jrs.20244006.

[43] D. R. I. M. Setiadi, "PSNR vs SSIM: Imperceptibility quality assessment for image steganography," *Multimedia Tools Appl.*, vol. 80, no. 6, pp. 8423–8444, Mar. 2021, doi: 10.1007/s11042-020-10035-z.

[44] G. M. Foody, D. S. Boyd, and M. E. J. Cutler, "Predictive relations of tropical forest biomass from Landsat TM data and their transferability between regions," *Remote Sens. Environ.*, vol. 85, no. 4, pp. 463–474, Jun. 2003, doi: 10.1016/S0034-4257(03)00039-7.

[45] V. R. Gharehbaghi, E. N. Farsangi, T. Y. Yang, and I. Hajirasouliha, "Deterioration and damage identification in building structures using a novel feature selection method," *Structures*, vol. 29, no. 10, pp. 458–470, Feb. 2021, doi: 10.1016/j.istruc.2020.11.040.

[46] N. R. Jachowski et al., "Mangrove biomass estimation in southwest Thailand using machine learning," *Appl. Geogr.*, vol. 45, pp. 311–321, Oct. 2013, doi: 10.1016/j.apgeog.2013.09.024.

[47] L. Breiman, "Random forests," *Mach. Learn.*, vol. 45, no. 1, pp. 5–32, Oct. 2001, doi: 10.1023/A:1010933404324.

[48] T. Lindner, J. Puck, and A. Verbeke, "Beyond addressing multicollinearity: Robust quantitative analysis and machine learning in international business research," *J. Int. Bus. Stud.*, vol. 53, no. 6, pp. 1–8, Jul. 2022, doi: 10.1057/s41267-022-00549-z.

[49] S. Chowdhury, Y. Lin, B. Liaw, and L. Kerby, "Evaluation of tree based regression over multiple linear regression for non-normally distributed data in battery performance," in *Proc. Int. Conf. Intell. Data Sci. Technol. Appl.*, San Antonio, TX, USA, 2002, pp. 17–25, doi: 10.1109/IDSTA55301.2022.9923169.

[50] Y. Zhu et al., "Estimating and mapping mangrove biomass dynamic change using WorldView-2 images and digital surface models," *IEEE J. Sel. Topics Appl. Earth Observ. Remote Sens.*, vol. 13, pp. 2123–2134, 2020, doi: 10.1109/JSTARS.2020.2989500.

[51] O. Mutanga, E. Adam, and M. A. Cho, "High density biomass estimation for wetland vegetation using WorldView-2 imagery and random forest regression algorithm," *Int. J. Appl. Earth Observ. Geoinf.*, vol. 18, pp. 399–406, Aug. 2012, doi: 10.1016/j.jag.2012.03.012.

[52] F. Cheng, G. Ou, M. Wang, and C. Liu, "Remote sensing estimation of forest carbon stock based on machine learning algorithms," *Forests*, vol. 15, no. 4, Apr. 2024, Art. no. 681, doi: 10.3390/f15040681.

[53] F. E. Fassnacht et al., "Importance of sample size, data type and prediction method for remote sensing-based estimations of aboveground forest biomass," *Remote Sens. Environ.*, vol. 154, pp. 102–114, Nov. 2014, doi: 10.1016/j.rse.2014.07.028.

[54] S. He, W. Wang, C. Zeng, and M. Liu, "Spatiotemporal pattern of economic development and the forecast in China," *Sci. Geographica Sinica*, vol. 36, no. 11, pp. 1622–1628, Nov. 2016, doi: 10.13249/j.cnki.sgs.2016.11.003.

[55] L. Zhao, Z. Zhao, and W. Wang, "The spatial pattern of economy in coastal area of China," *Econ. Geogr.*, vol. 34, no. 2, pp. 14–19, Feb. 2014, doi: 10.3969/j.issn.1000-8462.2014.02.003.

[56] X. Lin, Z. Li, W. Chen, X. Sun, and D. Gao, "Forest fire prediction based on long- and short-term time-series network," *Forests*, vol. 14, no. 4, Apr. 2023, Art. no. 778, doi: 10.3390/f14040778.

[57] F. Zhou and X. Wang, "Application of machine learning algorithms in analyzing the driving factors of forest fire occurrence in Guangxi and prediction of forest fires," *J. Northeast Forestry Univ.*, vol. 52, no. 11, pp. 72–82, Nov. 2024, doi: 10.13759/j.cnki.dlxb.2024.11.003.

[58] C. Yue, Y. Tang, T. Xu, and H. Xu, "Estimation of net primary productivity based on remote sensing and geographic information system in Shangri-La county," *J. Central South Univ. Forestry Technol.*, vol. 34, no. 7, pp. 90–98, Mar. 2014, doi: 10.14067/j.cnki.1673-923x.2014.07.001.

[59] M. E. Dusenge et al., "Boreal conifers maintain carbon uptake with warming despite failure to track optimal temperatures," *Nature Commun.*, vol. 14, Aug. 2023, Art. no. 4667, doi: 10.1038/s41467-023-40248-3.

[60] Y. Liao, J. Zhang, R. Rui, and D. Xu, "Estimating the dynamic changes of aboveground biomass of *Pinus densata* based on Landsat," *J. Southwest Forestry Univ.*, vol. 43, no. 1, pp. 117–125, Jan. 2023, doi: 10.11929/j.swfu.202111058.
[61] D. Han et al., "Improving *Pinus densata* carbon stock estimations through remote sensing in Shangri-La: A nonlinear mixed-effects model integrating soil thickness and topographic variable," *Forests*, vol. 15, no. 2, Feb. 2024, Art. no. 394, doi: 10.3390/f15020394.
[62] C. Yue, *Forest Biomass Estimation in Shangri-La County Based on Remote Sensing*. Beijing, China: Beijing Forestry Univ., 2009.
[63] J. Wang, F. Cheng, S. Xu, X. Wang, and F. Cheng, "Forest biomass estimation in Shangri-La based on the remote sensing," *J. Zhejiang Agriculture Forestry Univ.*, vol. 30, no. 3, pp. 325–329, May 2013, doi: 10.11833/j.issn.2095-0756.2013.03.003.
[64] C. Chen et al., "Estimation of above-ground biomass for *Pinus densata* using multi-source time series in Shangri-La considering seasonal effects," *Forests*, vol. 14, no. 9, Aug. 2023, Art. no. 1747, doi: 10.3390/f14091747.
[65] L. Luo and J. Zhang, "Aboveground biomass dynamics of *Pinus densata* in Shangri-La based on Landsat," *Forest Inventory Plan.*, vol. 48, no. 6, pp. 7–12, Nov. 2023, doi: 10.3969/j.issn.1671-3168.2023.06.002.
[66] Y. Liao, J. Zhang, R. Bao, D. Xu, and D. Han, "Modelling the dynamics of carbon storages for *Pinus densata* using Landsat images in Shangri-La considering topographic factors," *Remote Sens.*, vol. 14, no. 24, Oct. 2019, Art. no. 6244, doi: 10.3390/rs14246244.
[67] X. Zhang, W. Jia, Y. Sun, F. Wang, and Y. Miu, "Simulation of spatial and temporal distribution of forest carbon stocks in long time series—Based on remote sensing and deep learning," *Forests*, vol. 14, no. 3, Feb. 2023, Art. no. 483, doi: 10.3390/f14030483.

Kai Huang received the B.S. degree in geographic information science from Guangzhou University, Guangzhou, China, in 2022. He is currently working toward the M.S. degree in cartography and geographic information systems with the College of Soil and Water Conservation, Southwest Forestry University, Kunming, China.

His research interest focuses on remote sensing of resources and environment.

Chenkai Teng received the M.S. degree in cartography and geographical information system in 2024 from the College of Soil and Water Conservation, Southwest Forestry University, Kunming, China, where he is currently working toward the Ph.D. degree in forest management with the College of Forestry.

His research interests include the estimation of forest carbon stock based on remote sensing and time-series filtering algorithm.

Jialong Zhang received the doctoral degree in forest management from Southwest Forestry University, Kunming, China, in 2019.

He is a Professor, a Doctoral Supervisor, a Visiting Scholar with McGill University, a "Young Top Talents" of Yunnan Provincial High Level Talent Training Support Program, and the Head of Forest Management Discipline with the College of Forestry (College of Asia-Pacific Forestry), Southwest Forestry University, Kunming, China. His main research interests include time-series remote sensing-based modeling of forest biomass/carbon storage/carbon sink, land use and cover change, and sustainable development of forests.

Rui Bao received the M.S. degree in forest management from the College of Forestry (College of Asia-Pacific Forestry), Southwest Forestry University, Kunming, China, in 2021.

He is currently with the Southwest Survey and Planning Institute of National Forestry and Grassland Administration. He is mainly involved in forest resource monitoring. His research interests include estimation of forest carbon stock based on remote sensing and time-series filtering algorithm.

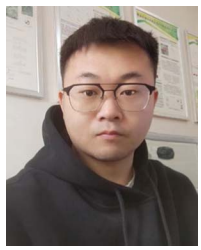

Yi Liao received the M.A. degree in forest management from the College of Forestry, Southwest Forestry University, Kunming, China, in 2022. He is currently working toward the doctoral degree in agricultural electrification and automation with the College of Mechanical and Electronic Engineering, Northwest Agriculture and Forestry University, Xianyang, China.

His research interests include forestry/agricultural remote sensing, forest biomass/carbon sinks, agricultural cropping structures, and agricultural carbon emissions.

Yunrun He received the M.S. degree in cartography and geographical information system in 2024 from the College of Soil and Water Conservation, Southwest Forestry University, China.

Her research interests include spatial heterogeneity of forest and forest AGB/ACS estimation.

Bo Qiu received the B.S. degree in civil engineering from Nanjing Technology University, Nanjing, China, in 2022. He is currently working toward the M.S. degree in forestry with the College of Forestry (College of Asia-Pacific Forestry), Southwest Forestry University, Kunming, China.

His research interest focuses on the estimation of forest carbon stock based on remote sensing.

Mingrui Xu received the B.S. degree in geographic information science in 2022 from Southwest Forestry University, Kunming, China, where she is currently working toward the M.S. degree in cartography and geographic information systems with the College of Soil and Water Conservation.

Her research interest focuses on remote sensing of resources and environment.